

Radiation Pressure-supported Accretion Disks: Vertical Structure, Energy Advection, and Convective Stability

Wei-Min Gu^{1,2}

guwm@xmu.edu.cn

ABSTRACT

By taking into account the local energy balance per unit volume between the viscous heating and the advective cooling plus the radiative cooling, we investigate the vertical structure of radiation pressure-supported accretion disks in spherical coordinates. Our solutions show that the photosphere of the disk is close to the polar axis and therefore the disk seems to be extremely thick. However, the profile of density implies that most of the accreted matter exists in a moderate range around the equatorial plane. We show that the well-known polytropic relation between the pressure and the density is unsuitable for describing the vertical structure of radiation pressure-supported disks. More importantly, we find that the energy advection is significant even for slightly sub-Eddington accretion disks. We argue that the non-negligible advection may help to understand why the standard thin disk model is likely to be inaccurate above ~ 0.3 Eddington luminosity, which was found by some works on the black hole spin measurement. Furthermore, the solutions satisfy the Solberg-Høiland conditions, which indicates the disk to be convectively stable. In addition, we discuss the possible link between our disk model and ultraluminous X-ray sources.

Subject headings: accretion, accretion disks — black hole physics — convection — hydrodynamics — instabilities

1. Introduction

The standard thin accretion disk model (Shakura & Sunyaev 1973) has been widely applied to X-ray binaries and active galactic nuclei. Due to the basic assumption of the energy

¹Department of Physics and Institute of Theoretical Physics and Astrophysics, Xiamen University, Xiamen, Fujian 361005, China

²Harvard-Smithsonian Center for Astrophysics, 60 Garden Street, Cambridge, MA 02138, USA

balance between the viscous heating and the radiative cooling, such a model was known to be invalid for super-Eddington accretion case, where the advective cooling is probably significant. Instead, the slim disk model (Abramowicz et al. 1988) was introduced to describe super-Eddington accretion disks. However, there exists some conflict between the theory and the observation. The theory predicts that the advection is negligible for $L \lesssim L_{\text{Edd}}$ (e.g., Watarai et al. 2000; Sądowski 2011), where L_{Edd} is the Eddington luminosity, which indicates that the standard disk model should be valid up to L_{Edd} . On the contrary, some works on the black hole spin measurement showed that the standard disk model is likely to be inaccurate for $L \gtrsim 0.3L_{\text{Edd}}$ (e.g., McClintock et al. 2006). Moreover, even the recent general model for optically thick disks (e.g., Sądowski 2011; Sądowski et al. 2011), which unifies the standard thin disk and the slim disk, could not help to obtain a self-consistent spin parameter for $L \gtrsim 0.3L_{\text{Edd}}$ (e.g., Straub et al. 2011). In our opinion, the above conflict may be resolved if the vertical structure is well incorporated.

Most previous works on accretion disks focused on the radial structure in cylindrical coordinates (R, ϕ, z) . For the vertical structure, however, a simple well-known relationship “ $H = c_s/\Omega_K$ ” or “ $H\Omega_K/c_s = \text{constant}$ ” was widely adopted, where H is the half-height of the disk, c_s is the sound speed, and Ω_K is the Keplerian angular velocity. Such a relationship comes from the vertical hydrostatic equilibrium with two additional assumptions. One is the approximation of gravitational potential: $\psi(R, z) \simeq \psi(R, 0) + \Omega_K^2 z^2/2$, and the other is a one-zone approximation or a polytropic relation $p_{\text{tot}} = \mathcal{K}\rho^{1+1/N}$ in the vertical direction (e.g., Hōshi 1977), where p_{tot} is the total (gas plus radiation) pressure and ρ is the density. Obviously, the above assumptions work well for geometrically thin disks, but may be inaccurate for the mass accretion rate \dot{M} approaching the Eddington one \dot{M}_{Edd} , for which the disk is probably not thin. Consequently, the relationship “ $H\Omega_K/c_s = \text{constant}$ ” may be invalid for $\dot{M} \gtrsim \dot{M}_{\text{Edd}}$.

Without the potential approximation, our two previous works investigated the geometrical thickness of accretion disks and the validity of the relationship “ $H\Omega_K/c_s = \text{constant}$ ”. Gu & Lu (2007) adopted the explicit gravitational potential in cylindrical coordinates and found that the above relationship is inaccurate for $\dot{M} \gtrsim \dot{M}_{\text{Edd}}$, and therefore the disk can be geometrically thick. Gu et al. (2009) took spherical coordinates to avoid the approximation of gravitational potential, and found that an advection-dominated accretion disk is likely to be quite thick. In these two works, however, the polytropic relation is still adopted in the vertical direction, which takes the place of the energy balance per unit volume between the viscous heating and the advective cooling plus the radiative cooling. The validity of such a polytropic relation, however, remains questionable, in particular for large \dot{M} due to dominant radiation pressure.

The purpose of this paper is to revisit the vertical structure of radiation pressure-supported disks by taking into account the local energy balance and to study the variation of energy advection with mass accretion rates. The paper is organized as follows. Equations and boundary conditions are derived in Section 2. A global view of the solutions in the \dot{m} - r diagram is presented in Section 3. For a typical radius $r = 10r_g$, the vertical structure and the energy advection are investigated in Section 4. The two-dimensional solutions and the convective stability are studied in Section 5. Summary and discussion are made in Section 6.

2. Equations and boundary conditions

2.1. Equations

We consider a steady state axisymmetric accretion disk in spherical coordinates (r, θ, ϕ) and use the Newtonian potential, $\psi = -GM/r$, where M is the black hole mass. Following Narayan & Yi (1995), we assume $v_\theta = 0$ for simplicity, which means a hydrostatic equilibrium in the θ direction. Simulations, (e.g., Ohsuga et al. 2005, Figure 3), however, revealed that v_θ will be significant for extremely high accretion rates such as $\dot{M} = 1000L_{\text{Edd}}/c^2$. As shown in the following sections, our solutions mainly correspond to \dot{M} around \dot{M}_{Edd} . For such accretion rates, the validity of $v_\theta = 0$ remains a question.

The basic equations of continuity and momentum take the forms (e.g., Kato et al. 2008):

$$\frac{1}{r^2} \frac{\partial}{\partial r} (r^2 \rho v_r) = 0 , \quad (1)$$

$$v_r \frac{\partial v_r}{\partial r} - \frac{v_\phi^2}{r} = -\frac{GM}{r^2} - \frac{1}{\rho} \frac{\partial p}{\partial r} + \frac{\kappa_{\text{es}}}{c} F_r , \quad (2)$$

$$-\frac{v_\phi^2}{r} \cot \theta = -\frac{1}{\rho r} \frac{\partial p}{\partial \theta} + \frac{\kappa_{\text{es}}}{c} F_\theta , \quad (3)$$

$$\frac{v_r}{r} \frac{\partial}{\partial r} (r v_\phi) = \frac{1}{\rho r^3} \frac{\partial}{\partial r} (r^3 \tau_{r\phi}) , \quad (4)$$

where v_r and v_ϕ are respectively the radial and azimuthal velocity, F_r and F_θ are respectively the radial and vertical radiation flux, p is the gas pressure, κ_{es} is the opacity of electron scattering, and $\tau_{r\phi}$ is the $r\phi$ component of the viscous stress tensor, $\tau_{r\phi} = \nu \rho r \partial(v_\phi/r)/\partial r$. Following the spirit of α stress prescription, we assume the kinematic viscosity coefficient $\nu = \alpha c_s^2 r / v_K$, where c_s is the sound speed defined below (Equation (7)), and $v_K = (GM/r)^{1/2}$ is the Keplerian velocity.

We would stress that, even though the α stress prescription has been widely adopted for theoretical studies, simulations of magnetorotational turbulence have shown that the stress

does not well scale locally with the pressure. For instance, the simulations on thin disks by a shearing box showed that, the time and box-averaged results are likely to support that the stress is proportional to the thermal (gas plus radiation) pressure (e.g., Hirose et al. 2009a, Figure 3). However, Figure 16 of Hirose et al. (2009b) shows that the maximal thermal pressure is located on the equatorial plane, whereas Figure 11 shows that the maximal stress is obviously not at the same place. These two figures reveal that the stress is not proportional to the pressure locally. In the present study, for simplicity, we will keep the local α stress prescription for numerical calculation, which is a weak point of this work.

The energy equation including gas and radiation is written as (e.g., Ohsuga et al. 2005)

$$\nabla \cdot [(e + E)\mathbf{v}] = -p\nabla \cdot \mathbf{v} - \nabla \mathbf{v} : \mathbf{P} - \nabla \cdot \mathbf{F} + \Phi_{\text{vis}} , \quad (5)$$

where e and E are the internal energy density of the gas and the radiation, respectively. $\mathbf{P} = \mathbf{f}E$ is the radiation pressure tensor, Φ_{vis} is the viscous dissipative function, and the radiation flux \mathbf{F} is expressed as

$$\mathbf{F} = -\frac{\lambda c}{\rho \kappa_{\text{es}}} \nabla E . \quad (6)$$

In this work, we focus on the region inside the photosphere, so we can take the well-known Eddington approximation, i.e., $\lambda = 1/3$ and the Eddington tensor $\mathbf{f} = \mathbf{I}/3$.

Since we only study the radiation pressure-supported disks, the gas pressure p and the gas internal energy density e will be dropped in our calculation. In order to avoid directly solving the partial differential equations, some assumptions on the radial derivatives ($\partial/\partial r$) are required. Following the spirit of self-similar assumptions (e.g., Begelman & Meier 1982; Narayan & Yi 1995), we adopt the following radial derivatives for c_s and E :

$$\frac{\partial \ln c_s}{\partial \ln r} = -\frac{1}{2} ; \quad \frac{\partial \ln E}{\partial \ln r} = -\frac{5}{2} ,$$

where the sound speed c_s is defined as

$$c_s^2 \equiv \frac{E}{3\rho} . \quad (7)$$

Based on the above two radial derivatives, the following four derivatives can be inferred from Equations (1)-(7):

$$\frac{\partial \ln |v_r|}{\partial \ln r} = -\frac{1}{2} ; \quad \frac{\partial \ln v_\phi}{\partial \ln r} = -\frac{1}{2} ; \quad \frac{\partial \ln \rho}{\partial \ln r} = -\frac{3}{2} ; \quad \frac{\partial \ln F_r}{\partial \ln r} = -2 .$$

With all the above derivatives, we can remove the “ $\partial/\partial r$ ” terms in Equations (2) and (4)-(6), and the following equations are then obtained from Equations (2)-(6):

$$\frac{1}{2}v_r^2 + \frac{5}{2}c_s^2 + v_\phi^2 - v_K^2 = 0 , \quad (8)$$

$$v_\phi^2 \cot \theta = -\frac{r\kappa_{\text{es}}}{c} F_\theta , \quad (9)$$

$$v_r = -\frac{3}{2} \frac{\alpha c_s^2}{v_K} , \quad (10)$$

$$-\frac{1}{2} v_r (3\rho v_\phi^2 - E) = \frac{1}{\sin \theta} \frac{d}{d\theta} (\sin \theta F_\theta) , \quad (11)$$

$$\frac{dE}{d\theta} = -\frac{3r\rho\kappa_{\text{es}}}{c} F_\theta , \quad (12)$$

$$F_r = \frac{5}{6} \frac{cE}{r\rho\kappa_{\text{es}}} . \quad (13)$$

The seven equations, Equations (7)-(13), enable us to solve for the seven variables: v_r , v_ϕ , c_s , ρ , E , F_r , and F_θ . There are two differential equations in this system. In addition, the position of the surface is unknown. Thus, totally three boundary conditions are required to determine a unique solution.

2.2. Boundary conditions

An obvious boundary condition on the equatorial plane is $F_\theta = 0$. However, this condition is not applicable for numerical calculation since it is automatically matched as indicated by Equation (9). Combining Equations (9) and (11) we can derive the following equation:

$$\cot \theta \frac{d}{d\theta} (v_\phi^2) = v_\phi^2 + \frac{rv_r\kappa_{\text{es}}}{2c} (3\rho v_\phi^2 - E) .$$

An alternative boundary condition on the equatorial plane is then obtained from the above equation (the left-hand side is zero thus the right-hand side should also be zero):

$$v_\phi^2 + \frac{rv_r\kappa_{\text{es}}}{2c} (3\rho v_\phi^2 - E) = 0 \quad (\theta = \frac{\pi}{2}) . \quad (14)$$

The second boundary condition is a definition of the surface. We define the photosphere as the position above which the optical depth is around unity. The condition can be written as

$$\tau_{\text{es}} \equiv r\kappa_{\text{es}}\rho^2 \left(\frac{d\rho}{d\theta} \right)^{-1} = 1 \quad (\theta = \theta_0) , \quad (15)$$

where θ_0 ($0 < \theta_0 < \pi/2$) is the polar angle of the photosphere. The third condition is related to the mass accretion rate:

$$\dot{M} = -2\pi r^2 \int_{\theta_0}^{\pi-\theta_0} \rho v_r \sin \theta \, d\theta . \quad (16)$$

3. Solutions in \dot{m} - r diagram

In our calculation we set $M = 10M_{\odot}$, $\kappa_{\text{es}} = 0.34 \text{ cm}^2\text{g}^{-1}$, and $\alpha = 0.02$, where the value of α is taken from recent simulations (Hirose et al. 2009a). The Eddington accretion rate is expressed as $\dot{M}_{\text{Edd}} = 4\pi GM/\eta c\kappa_{\text{es}}$, where η is a radiative efficiency of the flow. We choose $\eta = 1/16$ since it is comparable to the Schwarzschild black hole efficiency of 0.057. The dimensionless accretion rate is defined as $\dot{m} \equiv \dot{M}/\dot{M}_{\text{Edd}}$.

With the equations and boundary conditions in Section 2, we can numerically derive the θ -direction distribution of physical quantities for a given \dot{m} at a certain radius r . The radiation pressure-supported disk solutions in the \dot{m} - r diagram are shown in Figure 1, where $r_g \equiv 2GM/c^2$ is the Schwarzschild radius. The parameter space is divided into three regions by two parallel solid lines, roughly with $\dot{m} \propto r$. The region above the upper solid line is denoted by “Outflow”, where we cannot find solutions. No solution exists probably due to the assumption of $v_{\theta} = 0$ in advance. In our view, a real flow located in this region may have $v_{\theta} \neq 0$ and the inflow accretion rate may decrease inward. The physical understanding could be that, for high accretion rates and particularly for the inner radii, the viscous dissipation may be sufficiently large such that the radiation pressure is too strong to be balanced by the gravitational force. Thus, outflows may be driven by the radiation pressure and the inflow \dot{m} drops inward. On the other hand, simulations of supercritical accretion flows (e.g., Ohsuga et al. 2005, Figure 6) showed that the inflow accretion rate roughly follows the $\dot{m} \propto r$ relationship for $\dot{m} = 1000L_{\text{Edd}}/c^2$ at $r_{\text{out}} = 500r_g$ (corresponding to $\dot{m} = 62.5$ due to the definition of \dot{M}_{Edd} with $\eta = 1/16$). The slope of the upper solid line in Figure 1, which may be regarded as maximal accretion rates due to our calculation, agrees well with the slope in the above simulations.

The region under the lower solid line is denoted by “Gas pressure”, where no solution is found either. In our understanding, it is probably because the gas pressure cannot be ignored in this region, which may be in conflict with the radiation pressure-supported assumption. We would point out that, the lower solid line in this diagram is higher than the well-known line which separates the inner and middle regions of standard thin disks (Shakura & Sunyaev 1973). The reason is that, the gas and radiation pressure are comparable for the latter, whereas the radiation pressure-supported disk may require the accretion rate to be higher such that the radiation pressure sufficiently dominate over the gas pressure, and therefore the effect of gas pressure on the vertical structure can be completely ignored.

The region between the two solid line, denoted by “Radiation pressure”, which means that the radiation pressure is completely dominated, corresponds to the solutions of our main interest in this work. In Section 4, we will focus on the vertical structure and the energy advection at a typical radius, $r = 10r_g$, as indicated by the vertical dashed line in

Figure 1. In Section 5, we will study the two-dimensional solutions for a typical accretion rate $\dot{m} = 0.6$ in the range $6r_g \leq r \leq 12r_g$ and $0 < \theta \leq \pi/2$, as indicated by the horizontal dot-dashed line. In addition, we would point out that for inner radii such as $3 \sim 5r_g$, the two solid lines in Figure 1 may deviate from a real black hole accretion system due to the Newtonian potential used in this work.

4. Solutions at a typical radius $r = 10r_g$

4.1. Vertical structure

In this section, we will focus on the solutions at a typical radius $r = 10r_g$. Figure 2 shows the vertical structure of the disk with $\dot{m} = 0.6$. In Figure 2(a), the dot-dashed, dotted, solid, and dashed lines show the vertical distribution of the dimensionless density (ρ/ρ_0), radial velocity (v_r/v_K), azimuthal velocity (v_ϕ/v_K), and sound speed (c_s/v_K), respectively, where ρ_0 is the density on the equatorial plane. It is seen that ρ significantly decreases, whereas c_s and $|v_r|$ increases, from the equatorial plane to the surface. In Figure 2(b), the solid line shows the variation of τ_{es} (defined in Equation (15)), where the photosphere ($\tau_{\text{es}} = 1$) is located at $\theta_0 \approx 4^\circ$, quite close to the polar axis. The disk seems to be extremely thick according to the position of the photosphere. However, the profile of ρ implies that most of the accreted matter exists in a moderate range around the equatorial plane, such as $\pi/4 < \theta < 3\pi/4$, which is more clear in Figures 4 and 5 (discussed below). The dashed line shows the variation of $|F_\theta|/cE$. There exists $|F_\theta|/cE \lesssim 1/3$ for the whole solution, which indicates that the Eddington approximation is valid and the solution is therefore self-consistent.

With a more general viscosity, Begelman & Meier (1982) studied a geometrically thick, radiation pressure-supported model for supercritical accretion disks. They showed that there exists a narrow empty funnel along the rotation axis with a half-opening angle $\lesssim 4^\circ$. As seen in our Figure 2(a), the density drops sharply close to the photosphere, thus a nearly empty funnel also seems to exist in our model. The difference is that, the disk surface in Begelman & Meier (1982) is the position where some physical quantities such as v_r diverges, whereas our surface is defined as the position where Equation (15) is matched, and no divergence appears in our solutions.

For a real disk with $\dot{m} = 0.6$, the photosphere may exist between $\theta = 45^\circ$ and the present result ($\approx 4^\circ$). Our argument is as follows. There are two possible reasons that may cause the present photosphere quite close to the polar axis. One is that we have ignored the radiation force from one side (e.g., $\theta = \theta_0$ and $0 < \phi < \pi$) to the other (e.g., $\theta = \theta_0$ and $\pi < \phi < 2\pi$). The other reason is that we consider only the $r\phi$ component of the stress tensor, which may

cause inaccurate results for small θ , such as strong shearing of the angular velocity Ω in the vertical direction, where $\Omega = v_\phi/(r \sin \theta)$. Nevertheless, the $r\phi$ component assumption may work well for moderate θ : $\pi/4 < \theta < 3\pi/4$. The fact that the surface condition could not be matched in the range $\pi/4 < \theta < 3\pi/4$ indicates that the half-opening angle of the disk ($\pi/2 - \theta_0$) is likely to be larger than $\pi/4$.

The profile of c_s in Figure 2(a) is quite different from that in the previous works with a vertical polytropic assumption (e.g., Hōshi 1977; Gu et al. 2009). Under the polytropic relation $p_{\text{tot}} = \mathcal{K}\rho^{1+1/N}$ (normally $1.5 \leq N \leq 3$, and for radiation pressure-dominated case, p_{tot} can be replaced by $E/3$), c_s will decrease continuously from the equatorial plane to the surface. The reason for the opposite behavior of c_s , as implied in Figure 2(a), is that ρ drops faster than E from the equatorial plane to the surface. Figure 3 shows the variation of the quantity $d \ln E / d \ln \rho$ with θ for $\dot{m} = 0.5$ (dashed line), $\dot{m} = 0.6$ (solid line), and $\dot{m} = 1$ (dotted line). If the polytropic relation works well, $d \ln E / d \ln \rho$ should be a constant of $1 + 1/N$. It is clearly shown in Figure 3 that, however, $d \ln E / d \ln \rho$ varies significantly with θ rather than being a constant. More importantly, $d \ln E / d \ln \rho < 1$ indicates that N is negative thus unacceptable. We therefore argue that the polytropic relation should be unsuitable for describing the vertical structure of radiation pressure-supported disks. Moreover, since the energy advection is relevant to c_s (e.g., $Q_{\text{adv}} \simeq \dot{M} c_s^2 / 2\pi R^2$ in Abramowicz et al. 1995, where Q_{adv} is the advective cooling rate per unit area), we may expect essentially different results on the strength of advection.

4.2. Energy advection

Figure 4 shows the variation of the vertically averaged advection factor f_{adv} with the mass accretion rate \dot{m} , where f_{adv} is defined as $f_{\text{adv}} \equiv Q_{\text{adv}}/Q_{\text{vis}}$. The quantities Q_{adv} and Q_{vis} are expressed as follows:

$$Q_{\text{adv}} = r \int_{\theta_0}^{\pi-\theta_0} q_{\text{adv}} \sin \theta \, d\theta, \quad (17)$$

$$Q_{\text{vis}} = r \int_{\theta_0}^{\pi-\theta_0} q_{\text{vis}} \sin \theta \, d\theta, \quad (18)$$

where $q_{\text{adv}} = -v_r E / 2r$ and $q_{\text{vis}} = -3\rho v_r v_\phi^2 / 2r$ are respectively the advective cooling rate and the viscous heating rate per unit volume, as implied by the left-hand side of Equation (11).

The solid line in Figure 4 corresponds to the total accretion rate integrating from θ_0 to $\pi - \theta_0$, as shown by Equation (16), whereas the dashed line corresponds to the specific

accretion rate integrating from $\theta = \pi/4$ to $\theta = 3\pi/4$, i.e.,

$$\dot{M}_{\pi/4} = -2\pi r^2 \int_{\pi/4}^{3\pi/4} \rho v_r \sin \theta \, d\theta . \quad (19)$$

The reason why we calculate for $\dot{M}_{\pi/4}$ is that the $r\phi$ stress assumption may work well for $\pi/4 < \theta < 3\pi/4$. As shown by the horizontal range of the solid and dashed lines, most of the accreted matter exists in this specific range, e.g., $\dot{m}_{\pi/4} = 0.52$ corresponding to $\dot{m} = 0.6$. The figure also shows that f_{adv} rapidly increases with increasing \dot{m} in the range $0.5 \lesssim \dot{m} \lesssim 1.1$. More importantly, the value of f_{adv} ($0.2 \lesssim f_{\text{adv}} \lesssim 0.8$) indicates that the energy advection is significant even for sub-Eddington accretion disks.

Such a result is quite different from the previous one, where advection was found to be significant only for super-Eddington accretion case. Watarai et al. (2000) introduced an elegant formula to describe the $\dot{M} - L$ relationship based on their numerical solutions under the well-known Paczyński-Wiita potential (Paczynski & Wiita 1980). Their Equations (15)-(19) imply that, for the position $r = 10r_g$, advection is negligible for $\dot{M} \lesssim 67L_{\text{Edd}}/c^2$ ($\sim 4\dot{M}_{\text{Edd}}$). For the whole disk, advection is negligible for $\dot{M} \lesssim 20L_{\text{Edd}}/c^2$ ($1.25\dot{M}_{\text{Edd}}$). Such a critical \dot{M} for the whole disk was confirmed by some recent global solutions under the general relativity. Figure 4.11 of Sądowski (2011) shows that advection is negligible for $L \lesssim L_{\text{Edd}}$ for any spin parameter a_* . For $a_* = 0$, i.e., the Schwarzschild black hole, the critical \dot{M} is just around \dot{M}_{Edd} . In our opinion, the different results on the advection between the above two works and ours are related to the different approach to describing the vertical structure.

A significant difference is that Watarai et al. (2000) and Sądowski et al. (2011) chose the cylindrical coordinates whereas we adopt the spherical coordinates. Of course, the final results should not depend on the coordinates used. However, as pointed out by Abramowicz et al. (1997), there are some interesting differences between the equations written in cylindrical and spherical coordinates. There is no centrifugal force in the z direction in cylindrical coordinates, whereas there is no gravitational force in the θ direction in spherical coordinates. Abramowicz et al. (1997) claimed that it is exactly this property that makes the spherical coordinates much better adapted for describing the flow near the black hole horizon. Here, we argue that the spherical coordinates should be more suitable for describing geometrically thick disks as follows. In cylindrical coordinates, in the z direction, whether with a polytropic relation between the pressure and the density (Watarai et al. 2000), or with the local energy balance (Sądowski et al. 2011), an approximation for the gravitational force, i.e., $\partial\psi/\partial z = \Omega_K^2 z$, was adopted for describing the vertical structure. Such an approximation will probably be invalid for $z/r \gtrsim 1$. In particular for $z \rightarrow \infty$, the approximate force goes to infinity whereas the real force ought to vanish. Thus, the cylindrical coordinates seem

unsuitable for studying geometrically thick disks. In other words, a geometrically thick disk solution in cylindrical coordinates may not be self-consistent. Sądowski et al. (2011) limited their solutions by $\dot{M} \leq 2\dot{M}_{\text{Edd}}$ probably due to this reason. As shown by their Figure 10, the maximal value of H/r for $\dot{M} = 2\dot{M}_{\text{Edd}}$ is ~ 0.4 . For higher \dot{M} , the value of H/r will be even larger thus the solution based on the approximate force may be inaccurate. On the contrary, in spherical coordinates, there is no need to make approximation for the gravitational force. The centrifugal force in the θ direction, which takes the place of the z -direction gravitational force in cylindrical coordinates, is derived in this work by solving the vertical differential equations. Thus, our approach to the vertical structure seems to be more reasonable.

We would agree that the solutions in Sądowski et al. (2011) are likely to be self-consistent since their H/r is significantly less than unity, in particular for the solutions with $\dot{M} \lesssim \dot{M}_{\text{Edd}}$. Then what are the reasons for the quantitative difference in the advection for $\dot{M} \lesssim \dot{M}_{\text{Edd}}$ between their solutions and ours? In our understanding, there exist three possible reasons as follows. First, as mentioned in Section 3 of Sądowski et al. (2011) for their numerical methods, the vertical structure is derived by a given advection factor f_{adv} in advance. The value of f_{adv} is probably obtained by solving the radial structure on the equatorial plane. Moreover, their f_{adv} is assumed to be uniform in the z direction. On the contrary, we obtain a varying f_{adv} by solving the vertical equations. As shown by our Figure 8, f_{adv} increases significantly with z . We can therefore expect that the vertically averaged f_{adv} at a cylindrical radius will also be significantly larger than that at $z = 0$, which may explain why our f_{adv} is larger than that in Sądowski et al. (2011). Second, Sądowski et al. (2011) assumed a uniform v_R and v_ϕ in the z direction, and used the Keplerian strain to calculate the viscous dissipation. In our method, however, we include varying v_r and v_ϕ in the vertical direction, and the viscous dissipation is calculated based on v_ϕ instead of v_K . Third, Sądowski et al. (2011) assumed $v_z = 0$ whereas we have $v_\theta = 0$. As stressed by Abramowicz et al. (1997), since the stationary accretion flows resemble quasi-spherical flows ($\theta_0 \approx \text{constant}$) much more than quasi-horizontal flows ($H \approx \text{constant}$), $v_\theta = 0$ may be a more reasonable approximation than $v_z = 0$. Moreover, the above three reasons may also be responsible for the different results in the convective stability, as will be discussed in Section 5.3.

4.3. Spin problem for $L \gtrsim 0.3L_{\text{Edd}}$

As mentioned in Section 1, some works on the black hole spin measurement showed that the standard thin disk model is likely to be inaccurate for $L \gtrsim 0.3L_{\text{Edd}}$ (e.g., McClintock et al. 2006; Straub et al. 2011). One explanation is that the inner disk edge is still located at the innermost stable circular orbit (ISCO), but its emission is shaded by the outer disk. Thus,

the inner disk radius obtained from the spectral fitting is not true. However, Weng & Zhang (2011) showed that the disks in black hole and neutron star X-ray binaries trace the same evolutionary pattern for $L \gtrsim 0.3L_{\text{Edd}}$. In addition, for the neutron star system XTE J1701-462, the boundary emission area maintains nearly constant despite the varying luminosity of the disk (Lin et al. 2009, Figure 17), which indicates that the neutron star’s surface is not shaded. Weng & Zhang (2011) therefore argued that the inner disk of the black hole system should not be shaded either due to the similar phenomenon. They suggested that the inner disk radius moves outward because of the increasing radiation pressure.

In our opinion, from the energy advection, it is easy to understand that the standard disk model seems to be inaccurate above $0.3L_{\text{Edd}}$. As revealed by the lines in Figure 4, f_{adv} is likely to be non-negligible (probably ~ 0.1) for $\dot{m} \sim 0.3$ at $r = 10r_g$. We would point out that, compared with the Paczyński-Wiita potential, the Newtonian potential in the present work may magnify the viscous heating rate at small radii such as $10r_g$, thus the real f_{adv} at $10r_g$ may be smaller than the values showed in Figure 4. On the other hand, for the same \dot{m} , since the viscous heating rate at a smaller radius such as $r = 5r_g$ will probably be larger than that at $r = 10r_g$, so does the advection factor. We can therefore expect that, even for the Paczyński-Wiita potential, the advection at the position close to the ISCO should be non-negligible for $\dot{m} \sim 0.3$. Consequently, the standard thin disk model, based on the energy balance between the viscous heating and the radiative cooling with the advective cooling being ignored, may be inaccurate.

4.4. Vertical height

Figure 2 shows that ρ decreases significantly with decreasing θ , and Figure 4 implies that most of the accreted matter exists in the range $\pi/4 < \theta < 3\pi/4$. In order to have a more clear view, we define an averaged dimensionless height as $\Delta\theta \equiv \Sigma/2r\rho_0$, where the surface density Σ takes the form:

$$\Sigma = r \int_{\theta_0}^{\pi-\theta_0} \rho \sin \theta \, d\theta . \quad (20)$$

Figure 5 shows the variation of f_{adv} with $\Delta\theta$ (solid line). Even though the photosphere is close to the polar axis, the averaged height $\Delta\theta$ is geometrically slim with $0.3 \lesssim \Delta\theta \lesssim 0.6$. Furthermore, the figure shows that f_{adv} increases with increasing $\Delta\theta$ or \dot{m} , which agrees with the classic picture. For quantitative comparison, we plot the function $f_{\text{adv}} = 1.5 \tan^2(\Delta\theta)$ (dashed line) in Figure 5 due to the relationship $f_{\text{adv}} \gtrsim (H/R)^2$ introduced by Abramowicz et al. (1995), which is equivalent to $f_{\text{adv}} \gtrsim \tan^2(\Delta\theta)$ here. It is seen that f_{adv} is

not well proportional to $\tan^2(\Delta\theta)$. In the range $0.6 < \dot{m} < 1.1$ or $0.3 < f_{\text{adv}} < 0.8$, however, we may regard the formula $f_{\text{adv}} = 1.5 \tan^2(\Delta\theta)$ as a rough approximation.

5. Two-dimensional solutions and convective stability

5.1. Two-dimensional solutions

In Section 4, we focus on the solutions at a typical radius $r = 10r_g$. In this section we will study the disk solutions for various radii. Since the vertical solutions are based on the assumptions of partial derivatives in the radial direction (presented in Section 2.1), it is necessary to derive vertical solutions for various radii to check whether these assumptions are self-consistent. Following the example solution in Figure 2, we study the two-dimensional solutions for $\dot{m} = 0.6$ in the range $6r_g \leq r \leq 12r_g$ and $0 < \theta \leq \pi/2$. Figure 6 shows the radial variations of c_s and E (solid lines) for five polar angles, i.e., $\theta = 90^\circ, 75^\circ, 60^\circ, 45^\circ$, and 30° . For comparison, the radial profile of v_K , which is proportional to $r^{-1/2}$, is shown in Figure 6(a), and an example slope of $\propto r^{-5/2}$ is shown in Figure 6(b). The figure shows that c_s and E behave roughly as $\propto r^{-1/2}$ and $\propto r^{-5/2}$, respectively, which agrees with the original assumptions of radial derivatives. As mentioned in Section 2.1, once the radial derivatives of c_s and E are given, the other ones can be inferred from Equations (1)-(7). Thus, we can expect that the radial derivatives of v_r , v_ϕ , ρ , and F_r in the two-dimensional solutions should also be in agreement with the assumptions. Our solutions are therefore likely to be self-consistent.

In our calculation, the location of the photosphere does not vary much with the radius, i.e., $\theta_0 \lesssim 5^\circ$ for various radii. As discussed in Section 4.1, the real position of the photosphere is likely to be located in the range $5^\circ < \theta_0 < 45^\circ$. We will make some comparison with simulations for the photosphere in Section 6. As shown in Figure 6, the derivatives of c_s and E deviate a little for $r \rightarrow 12r_g$ and $\theta = 90^\circ$. Such a divergence may be well understood from Figure 1, which shows that the solution for $\dot{m} = 0.6$ and $r \rightarrow 12r_g$ is quite close to the lower solid line, which indicates that the gas pressure may not be negligible. In particular for the equatorial plane, the mass density has the maximal value there, thus the gas pressure may be most significant at this position.

5.2. Solberg-Høiland conditions

In this section, we will study the convective stability of the radiation pressure-supported disks. The well-known Solberg-Høiland conditions in cylindrical coordinates (R, ϕ, z) take

the forms (e.g., Tassoul 2000):

$$\frac{1}{R^3} \frac{\partial l^2}{\partial R} - \frac{1}{C_P \rho} \nabla P \cdot \nabla S > 0 , \quad (21)$$

$$-\frac{\partial P}{\partial z} \left(\frac{\partial l^2}{\partial R} \frac{\partial S}{\partial z} - \frac{\partial l^2}{\partial z} \frac{\partial S}{\partial R} \right) > 0 , \quad (22)$$

where l is the specific angular momentum per unit mass, P is the total pressure, C_P is the specific heat at constant pressure, and S is the entropy expressed as

$$dS \propto d \ln \left(\frac{P}{\rho^\gamma} \right) , \quad (23)$$

where γ is the adiabatic index.

The R and z components of the well-known Brunt-Väisälä frequency are written as

$$N_R^2 = -\frac{1}{\gamma \rho} \frac{\partial P}{\partial R} \frac{\partial}{\partial R} \ln \left(\frac{P}{\rho^\gamma} \right) ,$$

$$N_z^2 = -\frac{1}{\gamma \rho} \frac{\partial P}{\partial z} \frac{\partial}{\partial z} \ln \left(\frac{P}{\rho^\gamma} \right) ,$$

and the epicyclic frequency takes the form:

$$\kappa^2 = \frac{1}{R^3} \frac{\partial l^2}{\partial R} .$$

Thus, the first Solberg-Høiland condition, Equation (21), can be simplified as

$$N_{\text{eff}}^2 \equiv N_R^2 + N_z^2 + \kappa^2 > 0 , \quad (24)$$

where N_{eff} is defined as an effective frequency. For accretion disks, there usually exists $\partial P / \partial z < 0$ (as shown in Figure 8), so the second Solberg-Høiland condition, Equation (22), reduces to

$$\Delta_{\iota S} \equiv \frac{\partial l^2}{\partial R} \frac{\partial}{\partial z} \ln \left(\frac{P}{\rho^\gamma} \right) - \frac{\partial l^2}{\partial z} \frac{\partial}{\partial R} \ln \left(\frac{P}{\rho^\gamma} \right) > 0 . \quad (25)$$

In numerical calculation, we adopt $P = E/3$ and $\gamma = 4/3$ according to the radiation pressure-supported assumption.

5.3. Convective stability

Based on the two-dimensional solutions for $\dot{m} = 0.6$ in Section 5.1, we can obtain the variations of physical quantities in cylindrical coordinates and therefore investigate the

convective stability by Equations (24)-(25). We take the cylindrical radius $R = 10r_g$ as a typical position to study the convective stability.

Figure 7 shows the z -direction variations of κ^2 , N_R^2 , N_z^2 , N_{eff}^2 , and Δ_{IS} , where the former four quantities are normalized by Ω_K^2 , and the last one is normalized by v_K^2 . The positive values for both N_{eff}^2 and Δ_{IS} indicate that the disk should be convectively stable. For the equatorial plane, the result of $N_{\text{eff}}^2 > 0$ can be inferred by Equation (15) of Narayan & Yi (1994), which revealed that the disk will always be convectively stable for $\gamma = 4/3$ at $z = 0$.

For further understanding the convectively stable results for $z > 0$, we plot Figure 8 to show the z -direction variations of ρ , E , l , $E/\rho^{4/3}$, and the advection factor f_{adv} . It is seen that ρ drops faster than E with increasing z , so the quantity $E/\rho^{4/3}$ increases with z . From Equation (23) we immediately have

$$\frac{\partial S}{\partial z} \propto \frac{\partial}{\partial z} \ln \left(\frac{E}{\rho^{4/3}} \right) > 0, \quad (26)$$

which is known as the Schwarzschild criterion for a constant angular velocity at a cylindrical surface ($\partial\Omega/\partial z = 0$), corresponding to the so-called barytropic flows where the pressure depends only on the density. As the dashed line in Figure 8 shows, the angular momentum l (or equivalently the angular velocity Ω) does not vary significantly with z . Thus, the convectively stable results are easy to understand from $\partial S/\partial z > 0$.

In a similar study (vertical structure based on the local energy balance) of the general model for optically thick disks, however, the disk was found to be convectively unstable (e.g., Sądowski et al. 2009, 2011). As interpreted by the three possible reasons in Section 4.2, the significant difference in the results between their works and ours is probably related to the different approach to describing the vertical structure. In addition, here we would mention two more details which may help to understand the difference in convective stability. First, the profiles of ρ and E in Figure 8 reveal that the absolute value of radial velocity $|v_r|$ increases with z ($|v_r| \propto E/\rho$ inferred from Equations (7) and (10)). Compared with the uniform v_R in Sądowski et al. (2011), our increasing $|v_r|$ with z may result in faster drop of ρ in the z direction (steeper slope of ρ) if we simply assume the mass supply to be comparable. Second, compared with Sądowski et al. (2011), the advection in our solutions is significantly stronger, which means that for the same \dot{m} thus comparable viscous heating rate, the vertical radiation flux F_z will be less in our results. Thus, E may decrease slower in the z direction (flatter slope of E) due to the less F_z and lower ρ (inferred from Equation (6)). As indicated by Equation (26), the flatter slope of E and the steeper slope of ρ will both make contribution to $\partial S/\partial z > 0$, and the disk is therefore likely to be convectively stable.

We would stress that, our solutions are limited by the radiation pressure-supported case. Thus, the present results cannot directly show the convective stability of disks for either the

gas pressure-supported case or the case of comparable gas and radiation pressure. Actually, we have made some additional calculation for thin disks in cylindrical coordinates to check the convective stability, following the method of Sądowski et al. (2011) but without considering advection. We found that the disk is convectively stable for the gas pressure-supported case, whereas the disk is convectively unstable for the case of radiation pressure being significant. Thus, we would agree with Sądowski et al. (2011) on the convectively unstable disks for moderate accretion rates such as $0.01 \sim 0.1 \dot{M}_{\text{Edd}}$, corresponding to significant radiation pressure and non-negligible gas pressure. Moreover, for $\dot{m} \lesssim 0.1$, the disk will be geometrically thin, thus there is no difference between the assumptions $v_\theta = 0$ and $v_z = 0$, and f_{adv} is probably negligible. As a consequence, the solutions of Sądowski et al. (2011) ought to be accurate.

Furthermore, as revealed by the profiles of E and ρ in Figure 8, $d \ln E / d \ln \rho$ is less than unity in the z direction. Following the argument in Section 4.1, the polytropic relation seems unsuitable either in the z direction. In addition, as shown in Figures 7 and 8, our example solution for $\dot{m} = 0.6$ at $R = 10r_g$ is terminated at $z/R = 0.66$. The reason is that the solutions in spherical coordinates is limited by $r = 12r_g$ (as shown by the horizontal dot-dashed line in Figure 1), which corresponds to $z/R = 0.66$ at $R = 10r_g$ in cylindrical coordinates.

5.4. Analysis of convective stability for $z \ll R$

For the region close to the equatorial plane, we can make some analysis of the convective stability by the Taylor expansion method. Obviously, we have $\partial S / \partial z = 0$ at $z = 0$ from symmetric conditions. Thus, for $z \ll R$, the value of $\partial S / \partial z$ can be estimated by the second-order derivative at $z = 0$:

$$\frac{\partial S}{\partial z} \approx z \frac{\partial^2 S}{\partial z^2} \quad (z \ll R) . \quad (27)$$

Based on Equations (7)-(12), we can eliminate v_r , E , and F_θ and therefore obtain a set of three equations for the three quantities v_ϕ , c_s , and ρ . By using the Taylor expansion method, together with the boundary condition of Equation (14), we derive the following three relationships for the second-order derivatives of v_ϕ , c_s , and ρ (the ram-pressure term in Equation (8) is ignored):

$$\begin{aligned} \frac{5c_s}{2} \frac{\partial^2 c_s}{\partial \tilde{\theta}^2} + v_\phi \frac{\partial^2 v_\phi}{\partial \tilde{\theta}^2} &= 0 , \\ \frac{1}{\rho} \frac{\partial^2 \rho}{\partial \tilde{\theta}^2} + \frac{2}{c_s} \frac{\partial^2 c_s}{\partial \tilde{\theta}^2} &= -\frac{v_\phi^2}{c_s^2} , \end{aligned}$$

$$\frac{3}{v_\phi} \frac{\partial^2 v_\phi}{\partial \tilde{\theta}^2} = \frac{1}{2\rho} \frac{\partial^2 \rho}{\partial \tilde{\theta}^2} + \frac{1}{c_s} \frac{\partial^2 c_s}{\partial \tilde{\theta}^2} + \frac{1}{v_\phi^2 - c_s^2} \left(v_\phi \frac{\partial^2 v_\phi}{\partial \tilde{\theta}^2} - c_s \frac{\partial^2 c_s}{\partial \tilde{\theta}^2} \right),$$

where $\tilde{\theta}$ is defined as $\tilde{\theta} = \pi/2 - \theta$, which is a small value in the analysis.

In our solutions we have $c_s^2 \ll v_\phi^2$ at $z = 0$, e.g., $c_s^2/v_\phi^2 = 0.16$ for $\dot{m} = 0.6$ at $R = 10r_g$. For the simple case with $c_s^2/v_\phi^2 \ll 1$, the above three relationships provide

$$\frac{\partial^2 \ln v_\phi}{\partial \tilde{\theta}^2} \approx -\frac{5}{16} \frac{v_\phi^2}{c_s^2}; \quad \frac{\partial^2 \ln c_s}{\partial \tilde{\theta}^2} \approx \frac{1}{8} \frac{v_\phi^4}{c_s^4}; \quad \frac{\partial^2 \ln \rho}{\partial \tilde{\theta}^2} \approx -\frac{1}{4} \frac{v_\phi^4}{c_s^4}.$$

The second-order derivative of entropy at $z = 0$ can therefore be derived by the following coordinate transformation:

$$\frac{\partial^2 S}{\partial z^2} \propto \frac{\partial^2}{\partial z^2} \ln \left(\frac{c_s^2}{\rho^{1/3}} \right) = \frac{1}{R^2} \frac{\partial^2}{\partial \tilde{\theta}^2} \ln \left(\frac{c_s^2}{\rho^{1/3}} \right) + \frac{1}{R} \frac{\partial}{\partial r} \ln \left(\frac{c_s^2}{\rho^{1/3}} \right) \approx \frac{1}{R^2} \left(\frac{1}{3} \frac{v_\phi^4}{c_s^4} - \frac{1}{2} \right) > 0. \quad (28)$$

Thus, Equations (27)-(28) indicate $\partial S/\partial z > 0$ for the region close to the equatorial plane. The disk in this region is therefore likely to be convectively stable.

6. Summary and discussion

In this paper, we have studied the vertical structure, energy advection, and convective stability of radiation pressure-supported disks in spherical coordinates. In the θ direction, we replaced the pressure-density polytropic relation by the local energy balance per unit volume between the viscous heating and the advective cooling plus the radiative cooling, and obtained the distribution of physical quantities such as ρ , v_r , v_ϕ , c_s , E , and F_θ . The photosphere was found close to the polar axis and therefore the disk seems to be extremely thick. However, most of the accreted matter exists in a moderate range around the equatorial plane such as $\pi/4 < \theta < 3\pi/4$. We showed that the polytropic relation is unsuitable for describing the vertical structure of radiation pressure-supported disks. More importantly, we found that the energy advection is significant even for slightly sub-Eddington accretion disks, which is quite different from the previous result that the advection is of importance only for super-Eddington accretion disks. We argued that, the non-negligible advection may help to understand why the standard thin disk model is likely to be inaccurate for $L \gtrsim 0.3L_{\text{Edd}}$. In addition, we studied the two-dimensional solutions to check our basic assumptions of radial derivatives, which indicates our solutions to be self-consistent. Furthermore, we investigated the convective stability of the disks in cylindrical coordinates by the two-dimensional solutions derived in spherical coordinates. The disk solutions satisfy the Solberg-Høiland conditions, which reveals that the disk ought to be convectively stable.

To our knowledge, there are mainly two series of simulations on optically thick accretion flows. One is three-dimensional, radiation magnetohydrodynamic (RMHD) simulations by a shearing box, which focused on thin disks (e.g., Hirose et al. 2006; Krolik et al. 2007; Hirose et al. 2009a,b). The other is two-dimensional, either radiation hydrodynamic (RHD) or RMHD simulations for global flows, which included thin disks and super-Eddington accretion flows (e.g., Ohsuga et al. 2005, 2009; Ohsuga & Mineshige 2011). We would like to compare our numerical results with the latter owing to the global, radiation pressure-supported, and geometrically not thin case. Ohsuga et al. (2005) studied RHD simulations in spherical coordinates with the α stress assumption for only the $r\phi$ component, for extremely high accretion rates $\dot{M} = 300, 1000$, and $3000L_{\text{Edd}}/c^2$. Moreover, Ohsuga & Mineshige (2011) studied RMHD simulations in cylindrical coordinates for $\dot{M} \sim 100L_{\text{Edd}}/c^2$. In our results, the position of the photosphere is quite close to the polar axis with $\theta_0 \lesssim 5^\circ$. As discussed in Section 4.1, the real position may exist in the range $5^\circ < \theta_0 < 45^\circ$. In the simulations, Ohsuga & Mineshige (2011) showed that the photosphere is around $z/R = 2.4$ corresponding to $\theta_0 \sim 23^\circ$. Ohsuga et al. (2005) did not mention the position of photosphere, but their Figure 4 for the density distribution reveals that the photosphere should exist at a certain θ_0 significantly less than 45° . Thus, we would express that, for accretion rates around and beyond \dot{M}_{Edd} , the photosphere may exist far from the equatorial plane with $\theta_0 < 45^\circ$.

In addition, we discuss the possible link between our disk model and ultraluminous X-ray sources. As shown by the upper solid line in Figure 1, there exists a maximal accretion rate \dot{m}_{max} varying with the radius. We argue that the possible upper limit of the accretion rate may help to understand why most ultraluminous X-ray sources (ULXs) are not in thermal dominant state. As mentioned in the review paper of Feng & Soria (2011), there may exist three classes of black holes in ULXs: normal stellar mass black holes ($\sim 10M_\odot$), massive stellar black holes ($\lesssim 100M_\odot$), and intermediate mass black holes ($10^2 - 10^4M_\odot$). A massive stellar black hole with a moderate super-Eddington accretion rate seems to account for most sources up to luminosities \sim a few 10^{40} erg s $^{-1}$. The slim disk model, which is the classic model for super-Eddington accretion disks, predicts a dominant thermal radiation from the disk. However, observations have shown that ULXs are not in the thermal dominant state except only a few sources such as M82 X-1 (Feng & Kaaret 2010) and HLX-1 (Davis et al. 2011). In our understanding, the radiation of ULXs may be interpreted by an optically thick disk with $\dot{m} \lesssim \dot{m}_{\text{max}}$ plus strong outflows. The disk will provide a thermal radiation, which is normally not dominant because of the moderate \dot{m}_{max} . On the other hand, the outflows may make contribution to the non-thermal radiation by the bulk motion Comptonization (Titarchuk & Zannias 1998) or through the jet of the radiation-pressure driven and magnetically collimated outflow (Ohsuga & Mineshige 2011).

The author is particularly grateful to Ramesh Narayan for constructive suggestions and beneficial discussions. The author also thanks Ivan Hubeny, Da-Bin Lin, Aleksander Sądowski, Lijun Gou, Yucong Zhu, and Shan-Shan Weng for helpful discussions, and the referee for providing useful comments to improve the paper. This work was supported by the National Natural Science Foundation of China under grants 11073015 and 10833002, the National Basic Research Program (973 Program) of China under grant 2009CB824800, and the scholarship from China Scholarship Council under grant 2009835057.

REFERENCES

- Abramowicz, M. A., Chen, X., Kato, S., Lasota, J.-P., & Regev, O. 1995, *ApJ*, 438, L37
- Abramowicz, M. A., Czerny, B., Lasota, J.-P., & Szuszkiewicz, E. 1988, *ApJ*, 332, 646
- Abramowicz, M. A., Lanza, A., & Percival, M. J. 1997, *ApJ*, 479, 179
- Begelman, M. C., & Meier, D. L. 1982, *ApJ*, 253, 873
- Davis, S. W., Narayan, R., Zhu, Y., et al. 2011, *ApJ*, 734, 111
- Feng, H., & Kaaret, P. 2010, *ApJ*, 712, L169
- Feng, H., & Soria, R. 2011, *New Astron. Rev.*, 55, 166
- Gu, W.-M., & Lu, J.-F. 2007, *ApJ*, 660, 541
- Gu, W.-M., Xue, L., Liu, T., & Lu, J.-F. 2009, *PASJ*, 61, 1313
- Hirose, S., Blaes, O., & Krolik, J. H. 2009a, *ApJ*, 704, 781
- Hirose, S., Krolik, J. H., & Blaes, O. 2009b, *ApJ*, 691, 16
- Hirose, S., Krolik, J. H., & Stone, J. M. 2006, *ApJ*, 640, 901
- Hōshi, R. 1977, *Prog. Theor. Phys.*, 58, 1191
- Kato, S., Fukue, J., & Mineshige, S. 2008, *Black-Hole Accretion Disks: Towards a New Paradigm* (Kyoto: Kyoto Univ. Press)
- Krolik, J. H., Hirose, S., & Blaes, O. 2007, *ApJ*, 664, 1045
- Lin, D., Remillard, R. A., & Homan, J. 2009, *ApJ*, 696, 1257
- McClintock, J. F., Shafee, R., Narayan, R., et al. 2006, *ApJ*, 652, 518

- Narayan, R., & Yi, I. 1994, ApJ, 428, L13
- Narayan, R., & Yi, I. 1995, ApJ, 444, 231
- Ohsuga, K., & Mineshige, S. 2011, ApJ, 736, 2
- Ohsuga, K., Mineshige, S., Mori, M., & Kato, Y. 2009, PASJ, 61, L7
- Ohsuga, K., Mori, M., Nakamoto, T., & Mineshige, S. 2005, ApJ, 628, 368
- Paczyński, B., & Wiita, P. J. 1980, A&A, 88, 23
- Sądowski, A. 2011, PhD thesis, arXiv:1108.0396
- Sądowski, A., Abramowicz, M., Bursa, M., et al. 2011, A&A, 527, A17
- Sądowski, A., Abramowicz, M., Bursa, M., et al. 2009, A&A, 502, 7
- Shakura, N. I., & Sunyaev, R. A. 1973, A&A, 24, 337
- Straub, O., Bursa, M., Sądowski, A., et al. 2011, A&A, 533, A67
- Tassoul, J.-L. 2000, *Stellar Rotation* (Cambridge: Cambridge Univ. Press)
- Titarchuk, L., & Zannias, T. 1998, ApJ, 493, 863
- Watarai, K.-Y., Fukue, J., Takeuchi, M., & Mineshige, S. 2000, PASJ, 52, 133
- Weng, S.-S., & Zhang, S.-N. 2011, ApJ, 739, 42

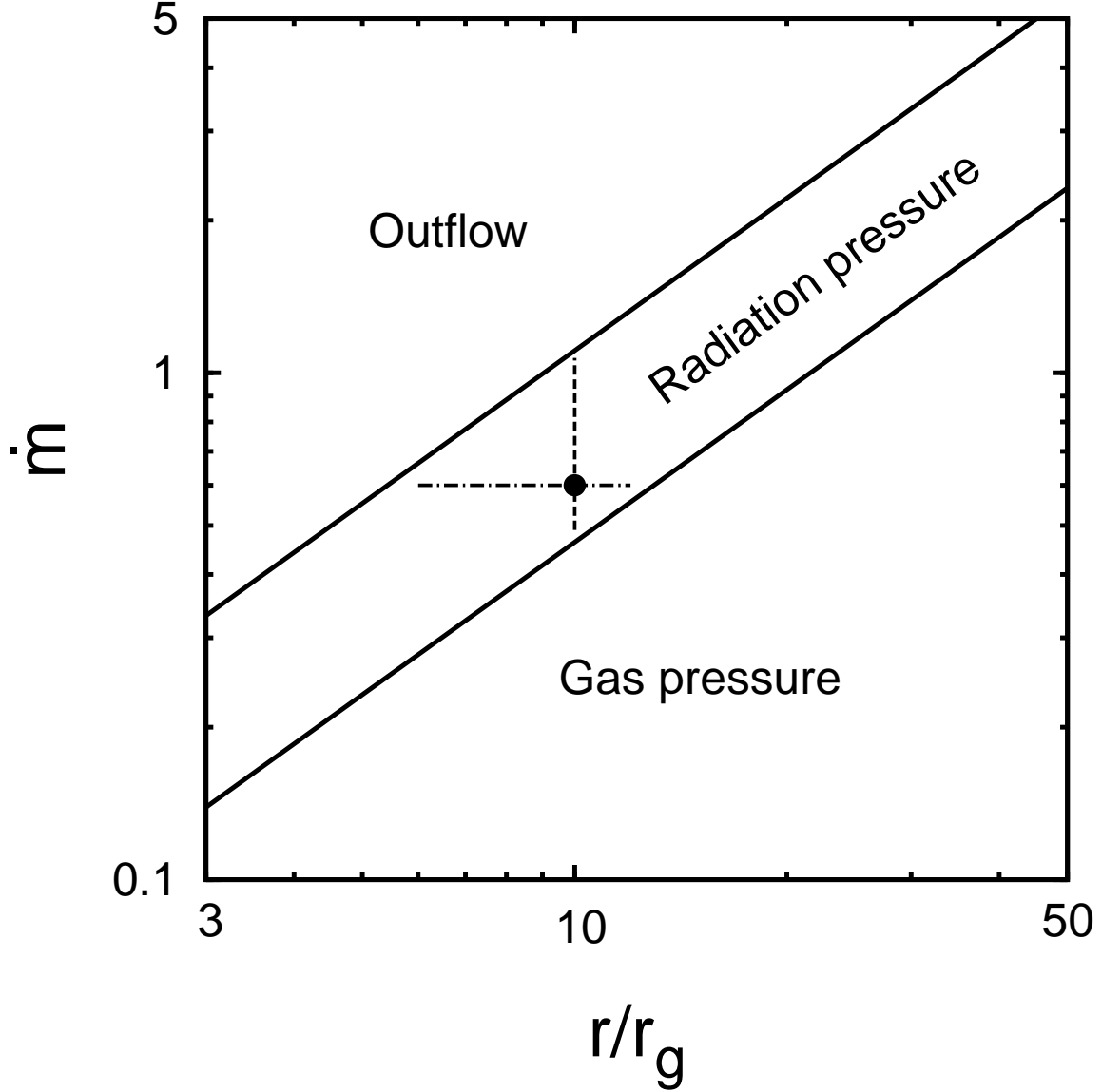


Fig. 1.— Solutions in the \dot{m} - r diagram. The parameter space is divided into three regions by two parallel solid lines. The middle region, denoted by “radiation pressure”, corresponds to the radiation pressure-supported disk, which is our main interest in this work. An example solution for $\dot{m} = 0.6$ at $r = 10r_g$ (filled circle) is shown in Figure 2. The solutions for various \dot{m} at a typical radius $r = 10r_g$ (vertical dashed line) are focused on in Section 4. The two-dimensional solutions for $\dot{m} = 0.6$ (horizontal dot-dashed line) are studied in Section 5.

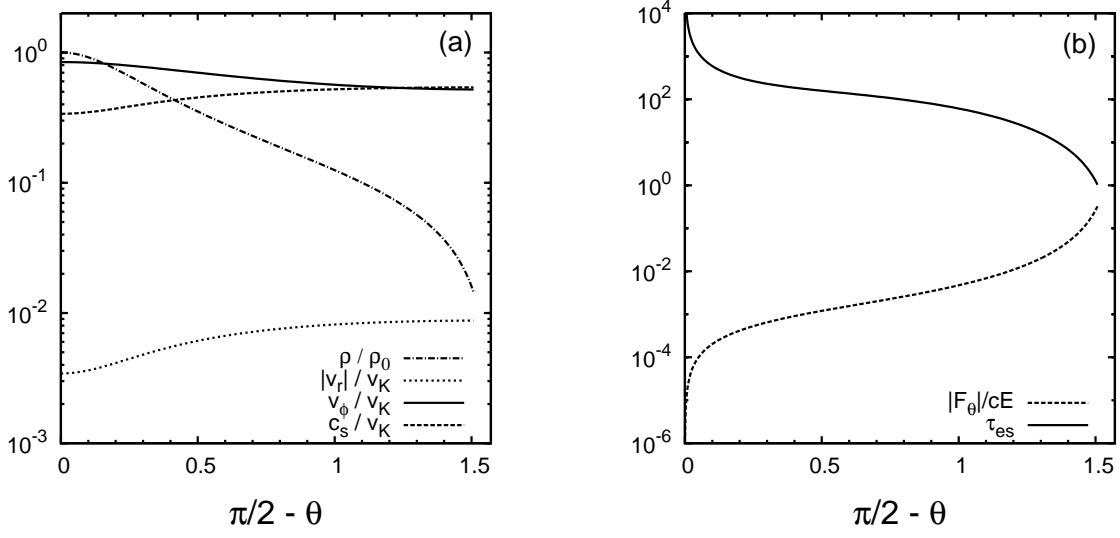


Fig. 2.— Vertical structure of the disk for $m = 0.6$ at $r = 10r_g$: (a) variations of ρ , $|v_r|$, v_ϕ , and c_s ; (b) variations of $|F_\theta|/cE$ and τ_{es} .

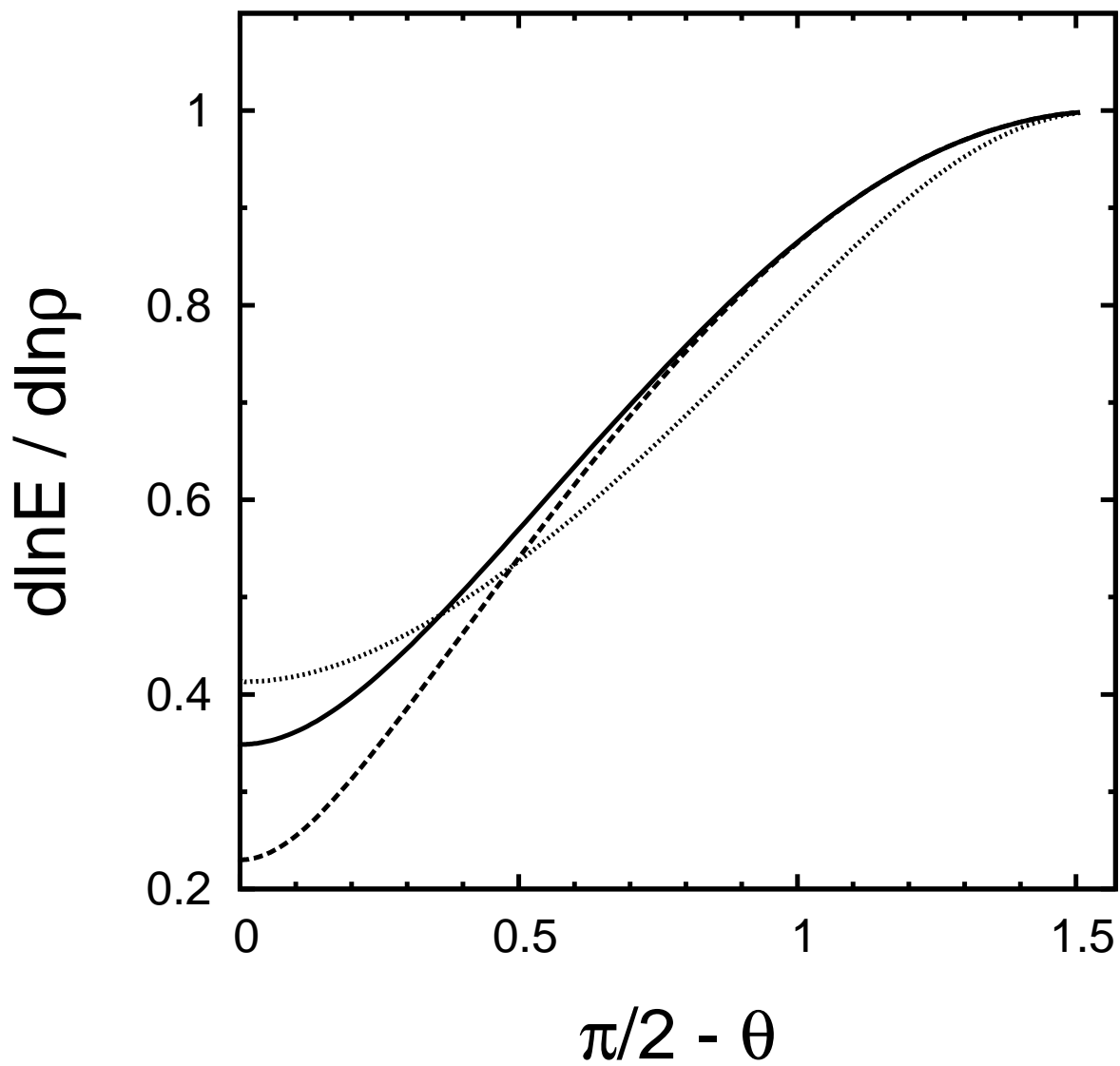


Fig. 3.— Vertical distribution of $d \ln E / d \ln \rho$ for $\dot{m} = 0.5$ (dashed line), $\dot{m} = 0.6$ (solid line), and $\dot{m} = 1$ (dotted line).

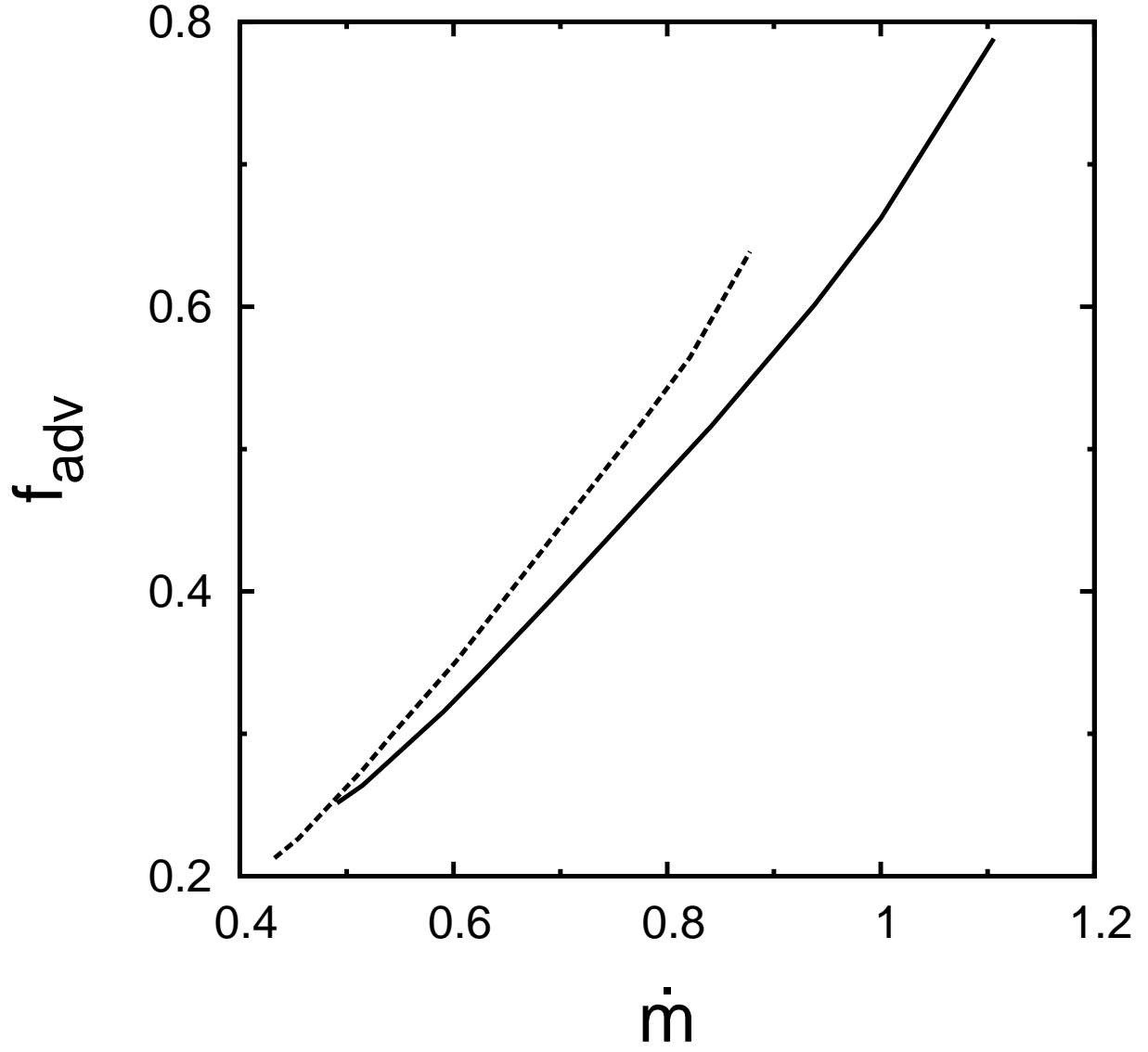


Fig. 4.— Variation of f_{adv} with \dot{m} (solid line) and $\dot{m}_{\pi/4}$ (dashed line).

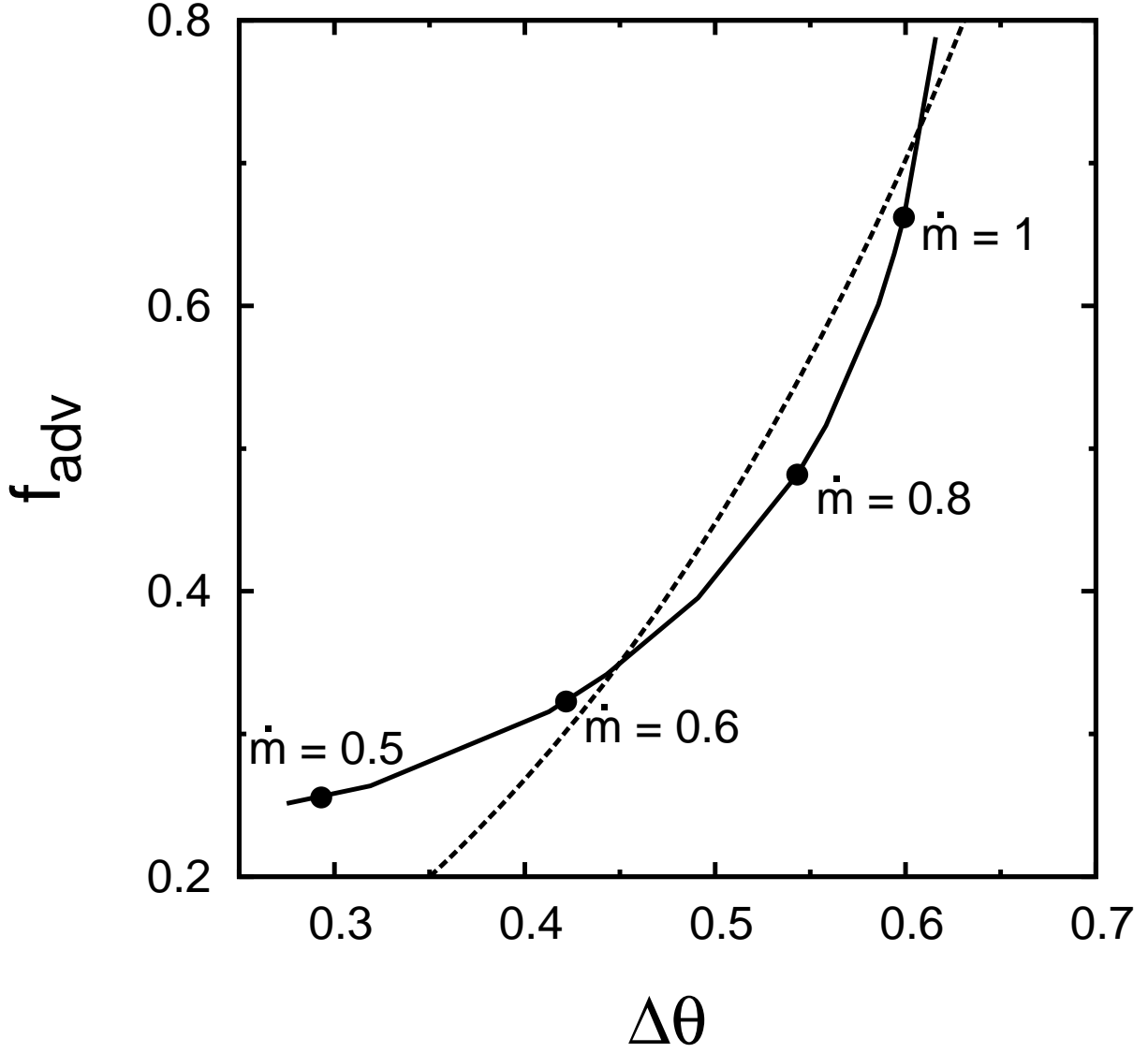


Fig. 5.— Variation of f_{adv} with the dimensionless height $\Delta\theta$ (solid line). For comparison, the function $f_{\text{adv}} = 1.5 \tan^2(\Delta\theta)$ is plotted (dashed line). The four typical accretion rates, $\dot{m} = 0.5, 0.6, 0.8$, and 1 , are denoted by filled circles.

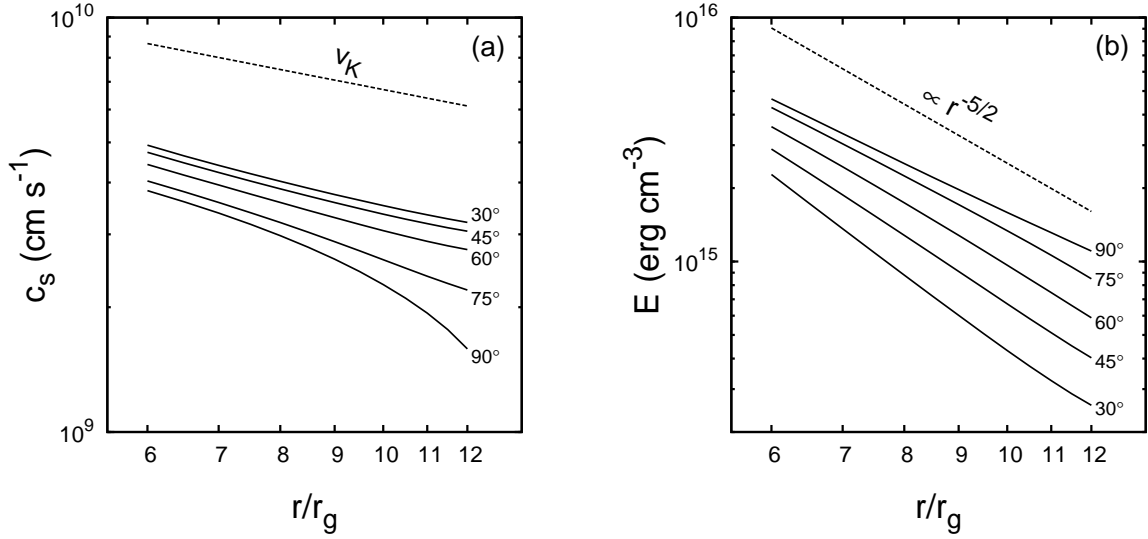


Fig. 6.— Radial variations of c_s and E (solid lines) for the polar angle $\theta = 90^\circ, 75^\circ, 60^\circ, 45^\circ$, and 30° for $\dot{m} = 0.6$. For comparison, the Keplerian velocity v_K ($\propto r^{-1/2}$) and an example slope of $\propto r^{-5/2}$ are plotted by the dashed lines in (a) and (b), respectively.

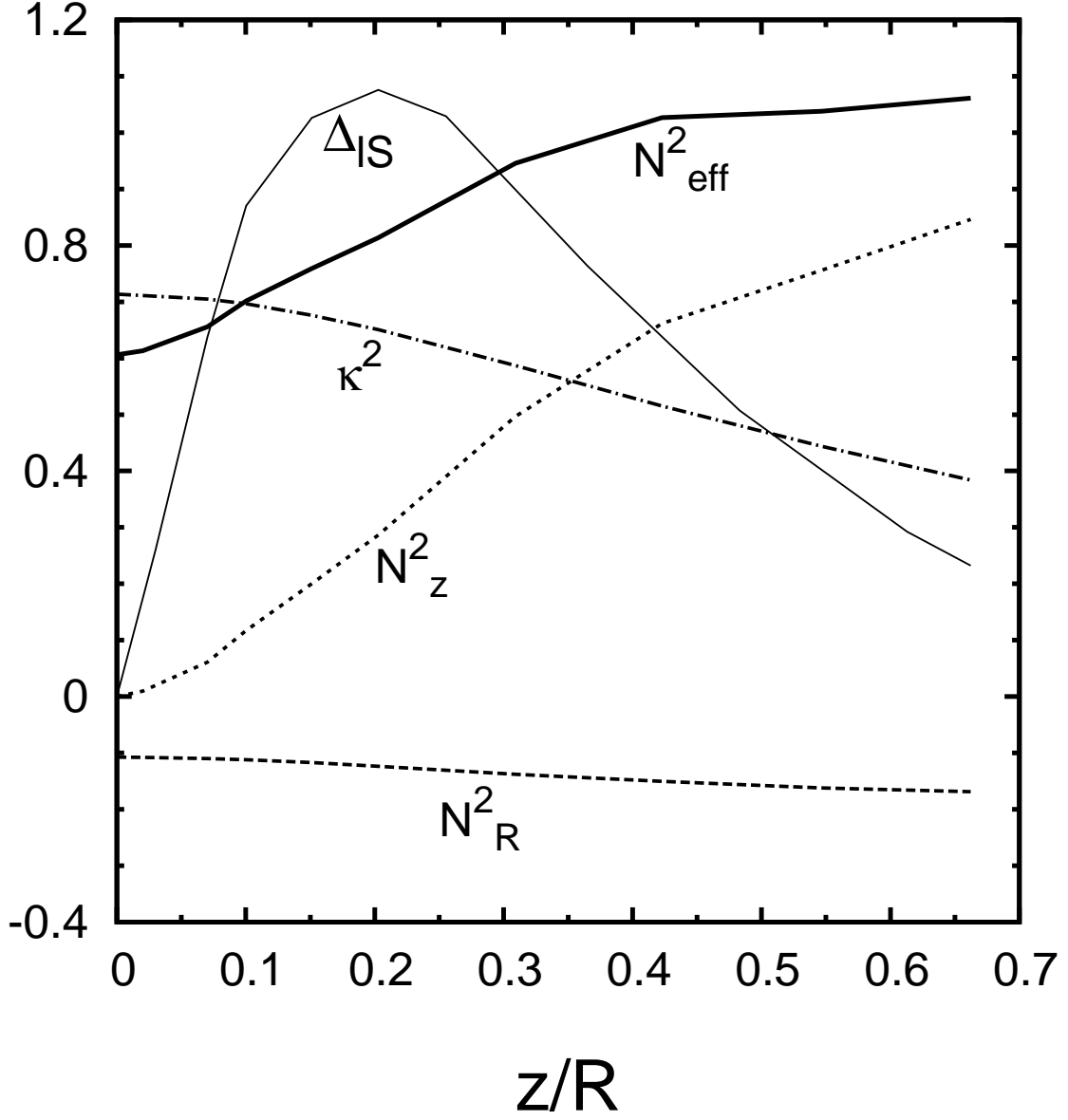


Fig. 7.— z -direction variations of κ^2 (dot-dashed line), N_R^2 (dashed line), N_z^2 (dotted line), N_{eff}^2 (thick solid line), and Δ_{IS} (thin solid line) for $\dot{m} = 0.6$ at a cylindrical radius $R = 10r_g$. The quantities κ^2 , N_R^2 , N_z^2 , and N_{eff}^2 are normalized by Ω_K^2 , and Δ_{IS} is normalized by v_K^2 .

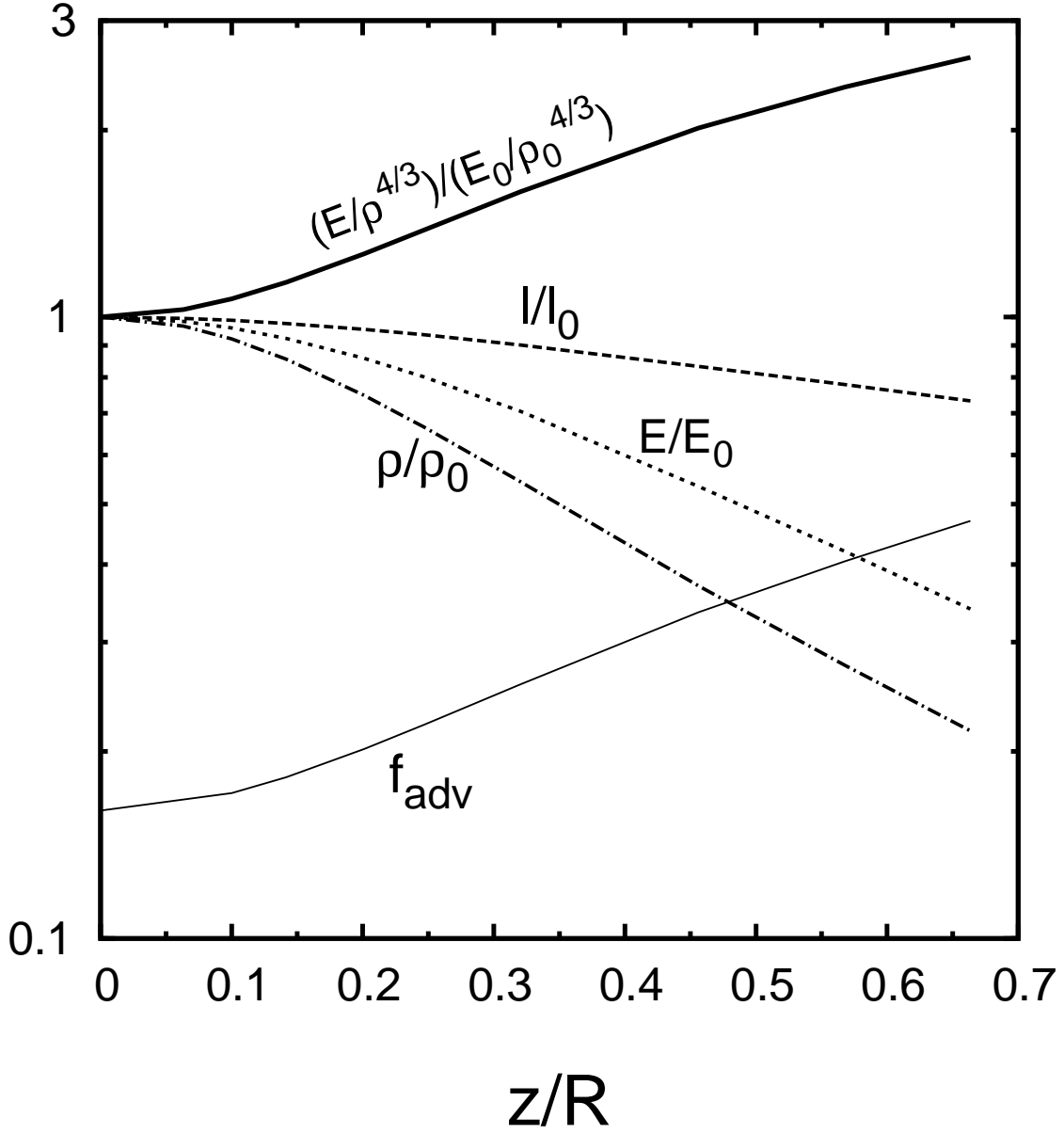


Fig. 8.— z -direction variations of $(E/\rho^{4/3})/(E_0/\rho_0^{4/3})$ (thick solid line), l/l_0 (dashed line), E/E_0 (dotted line), ρ/ρ_0 (dot-dashed line), and f_{adv} (thin solid line) for $\dot{m} = 0.6$ at $R = 10r_g$, where the subscript “0” represents the quantities on the equatorial plane.